RSC Advances

PAPER

View Article Online
View Journal | View Issue

Check for updates

Cite this: *RSC Adv.*, 2022, **12**, 14610

Morphological characteristics of calcium carbonate crystallization in CO_2 pre-cured aerated concrete

Jiayu Lu,[a] Shengqian Ruan,[a] Yi Liu,[b] Tao Wang,[c] Qiang Zeng *[a] and Dongming Yan*[a]

Received 24th March 2022
Accepted 8th May 2022

DOI: 10.1039/d2ra01901a

rsc.li/rsc-advances

Early-stage CO_2 curing technology for alkaline construction materials (such as cement concrete) has gained increasing interest owing to the advantages of material properties improvement and high potential of CO_2 sinking. Less attention, however, has been paid to morphological characteristics of $CaCO_3$ in carbonated cement concrete. The crystal structure and micromorphology of $CaCO_3$ in an early-age aerated concrete (AC) cured under CO_2 gas pressures of 0.1, 1, and 2 bar were investigated. The fabricated AC has a high CO_2 sorption capacity (~35 g CO_2 per 100 g cement in a 100 mm cube). The morphological characteristics of $CaCO_3$ were statistically analyzed in terms of long-axis length (*b*), short-axis length (*a*), and aspect ratio ($K = b/a$). As CO_2 pressure increases, *b* is almost unchanged from 0.8–1.8 μm, *a* decreases from 0.7 to 0.4 μm, and, consequently, *K* increases from 1.3 to 2.5. The different $CaCO_3$ crystal morphologies in AC are ascribed to the CO_2 pressure-associated crystal transformation processes: low gas pressure induces a symmetric $CaCO_3$ growth, while high gas pressure causes a faster calcite growth at the crystal tip ends. The findings would deepen the understanding of $CaCO_3$ crystal formation under different CO_2 curing pressures for tuning the microstructure of CO_2-cured cement concrete.

Open Access Article. Published on 13 May 2022. Downloaded on 7/2/2025 11:34:50 PM.
This article is licensed under a Creative Commons Attribution-NonCommercial 3.0 Unported Licence.

1. Introduction

Building materials industry is one of the industrial sectors with the largest energy consumption and carbon emissions (accounting for approximately 14.4% of the total carbon emissions) in China.[1,2] In recent years, the high potential of carbon sequestration by building materials has attracted increasing attention in both scientific and industrial communities. Most alkaline cementitious materials, such as Portland cement, blast furnace slag, and fly ash, can absorb CO_2, and carbonation reaction processes generally result in progressive alkali decrease or neutralization.[3–6] Carbon fixation may enhance the cementitious ability when alkaline oxides, such as calcium oxide (CaO) and magnesium oxide (MgO), in building materials react with CO_2 to generate insoluble and stable carbonates. Current knowledge indicates that CO_2 treatment of cement-based materials (CBMs) at early age can not only absorb a large amount of CO_2 but also refine the microstructure and improve mechanical properties and durability performances.[7–12] Experimental tests evidenced that the early-age carbonation of CBMs enables CO_2 absorption of 6.2–22.82%, and the 1d strength increases by around 20%.[13–17] The formation of $CaCO_3$ crystals and/or amorphous calcium carbonate (ACC) can fill pores in meso and micro sizes, which enhances the material's microstructure.[9,18,19] Consequently, improvements in resistance to chloride migration, gas penetration,[20] freeze-thaw, sulfate erosion, and dry–wet cycles have been reported for early-age carbonated CBMs.[21–25]

Many factors can affect early carbonation curing of CBMs, such as, raw materials, water–cement ratio, carbonation time, and temperature, among which the gas pressure of CO_2 (or concentration) may be the most important factor.[26] Generally, to accelerate the carbonation of alkaline active minerals in CBMs, relatively high CO_2 gas pressures (between 0.1–0.5 MPa) are recommended.[17] In the physical and chemical context, CO_2 gas pressure can significantly impact the diffusion and reaction rate of CO_2 molecules in cement-based materials. Shi *et al.* found that when the pressure of CO_2 gas increased from 10 to 60 psi (0.069–0.414 MPa), carbon absorption increased by nearly 1.7 times, and the compressive strength did not significantly change.[27] Kottititum *et al.* found that when the curing pressure was increased from 1 to 3 bar (0.1–0.3 MPa), the modulus of rupture of fiber–cement composites increased by 16%, the modulus of elasticity increased by 23%, and the toughness decreased by 51%.[28] Tu *et al.* observed that CO_2 pressure (0.01 and 0.4 MPa) impacted the crystalline of $CaCO_3$ for cement specimens mixed with limestone powder.[29]

[a]*College of Civil Engineering and Architecture, Zhejiang University, 866 Yuhangtang Road, Hangzhou, Zhejiang, 310058, China. E-mail: cengq14@zju.edu.cn; dmyan@zju.edu.cn*

[b]*Institute for Composites Science Innovation (InCSI), School of Materials Science and Engineering, Zhejiang University, 38 Zheda Road, Hangzhou, Zhejiang, 310027, China*

[c]*State Key Laboratory of Clean Energy Utilization, Zhejiang University, 38 Zheda Road, Hangzhou, Zhejiang, 310027, China*

© 2022 The Author(s). Published by the Royal Society of Chemistry

Open Access Article. Published on 13 May 2022. Downloaded on 7/2/2025 11:34:50 PM. This article is licensed under a Creative Commons Attribution-NonCommercial 3.0 Unported Licence.

Extensive reports have supported the multiple benefits of carbonation to CBMs at early ages in terms of CO_2 sinking and engineering performance improvement. Different $CaCO_3$ crystal structures have been reported in different experiments.[30–34] Calcite has been observed in most experiments of carbonation of CBMs.[35–38] Insufficient attention, however, has been paid to morphological characteristics of $CaCO_3$ in carbonated cement concrete. Significant diversity in the microstructure and morphology of $CaCO_3$ crystals in carbonated CBMs has been reported. Jian *et al.* explored the morphological diversity, growth mechanism, and shape evolution of $CaCO_3$ crystals in cement with dilute hydration through scanning electron microscopy (SEM) and first-principles calculation.[39] The authors suggested that the $[Ca^{2+}]$-to-$[CO_3^{2-}]$ ratio in a cement system may be the principal cause of crystal morphological diversity according to the theory of aqueous chemistry. However, the formation of crystals in diluted hydrated cement may not be representative of the carbonation of real CBMs with relatively dense microstructures. Monkman and Shao observed granular, lath-like $CaCO_3$ crystals (with a size of approximately 1 μm) agglomerated tightly on the surface of cement particles, filling the spaces between particles in the cement samples, and irregularly shaped and loosely distributed carbonation products on the substrate in the slag and fly ash samples.[16] Siauciunas *et al.* observed that during the carbonation process, $CaCO_3$ grew from amorphous particles of several hundred nanometers into layered and rhombohedral of 1–2 μm.[40] Li *et al.* found that cube granular or rod-shaped crystals were embedded in the hydration product, calcium-silicate-hydrates (C–S–H), to improve the integrity and compactness of the structure.[41] Qin *et al.* reported irregular granular $CaCO_3$ crystals in cement–coal gangue paste.[24] In a wellbore cement sample, euhedral hexagonal prisms $CaCO_3$ crystals with a width of 10–20 μm and trigonal symmetry have been reported.[20] The aforementioned examples of large diversity in the microstructure and morphology of $CaCO_3$ crystals have evidenced wide gaps between the state-of-the-art knowledge of carbonation mechanisms and the alterations to engineering performance of CBMs after early-age carbonation.

To narrow the gaps, it is essential to unravel the morphological characteristics of $CaCO_3$ in CBMs subjected to early-age carbonation and the mechanisms of $CaCO_3$ growth in materials with complex microstructures. A parallel aim of this work is to clarify the impact of CO_2 gas pressure on the microstructure and mineral morphology of $CaCO_3$ in CO_2-cured cement concrete. Here, thermogravimetric analysis (TGA), X-ray diffraction (XRD), Fourier-transform infrared spectroscopy (FTIR), and SEM tests were used to characterize the chemical and morphological characteristics of aerated concrete (AC) blocks cured at CO_2 gas pressures of 0.1, 1, and 2 bar (0.01, 0.1 and 0.2 MPa). Geometrical parameters of $CaCO_3$ (*i.e.*, long-and short-axis lengths, and the aspect ratio) were statistically evaluated on the basis of imaging analysis. Profound discussions on CO_2 gas pressure-associated carbonation mechanisms were performed. The findings of this work would deepen the understanding of $CaCO_3$ morphology and carbonation mechanisms of CBMs at different CO_2 curing pressures, which would help tune the microstructure of CO_2-cured cement concrete toward better manipulation of CO_2 sinking and engineering performance of CBMs.

2. Experimental program

2.1 Materials and mix proportion

The AC was fabricated for early-age carbonation. The porous structure of AC facilitates rapid gas and moisture diffusion in AC specimens, enabling rapid CO_2 sinking.[42] Ordinary Portland cement (Type P·O 42.5) from Anhui Conch Cement Co., Ltd., China, was used as the main binding material for AC specimen fabrication. Two industrial wastes, *i.e.*, Class C fly ash from Hangzhou Hanglian thermal power plant, Zhejiang, China, and ground granulated blast furnace slag (GGBFS) from Henan Anyang Iron & Steel Group Co., Ltd., Henan, China, were used to improve the sustainability of AC. The advantages of adding fly ash and GGBFS to AC include low density, improving thermal insulation performance, and providing calcareous material for carbon absorption.

The chemical composition of the raw materials was collected by X-ray fluorescence, XRD, and a laser particle size analyzer. Cement, GGBFS, and fly ash contain 57.61%, 33.83%, and 17.58% CaO, respectively, which could be carbonized and converted into $CaCO_3$ (Table 1). In addition, the slag also contains a certain amount of MgO (7.74%, see Table 1).

Fig. 1 demonstrates the crystalline phases of solid materials tested by XRD. The cement mainly contains tricalcium silicate (C_3S), dicalcium silicate (C_2S), tricalcium aluminate (C_3A), tetra calcium aluminoferrite (C_4AF), and gypsum. The hump of the slag curve indicates the presence of several amorphous substances, and the crystals that can be distinguished are carbonates. Quartz (SiO_2), anhydrite ($CaSO_4$), lime (CaO), portlandite ($Ca(OH)_2$), calcite ($CaCO_3$), and magnesium calcite ($Mg_{0.03}Ca_{0.97}(CO_3)$) crystals are detected in fly ash (Fig. 1).

Fig. 2 shows the particle size distribution of raw materials. The cement and fly ash share a similar particle size distribution with a 50% volume size of 17 μm, whereas GGBFS has coarser particle sizes with a 50% volume size of 49 μm.

Aluminum powder from Huai'an Jiayi Building Material Co., Ltd., Jiangsu, China was used for gas generation, and additional gypsum from Sinopharm Chemical Reagent Co., Ltd., Shanghai, China, was used to balance gas generation rates, preventing excessive swelling. Specific AC mixture proportions are listed in Table 2.

2.2 Specimen preparation

AC concrete specimens were prepared as follows. First, the aluminum powder was mixed with deionized water in a ratio of 1 : 5 with low-speed stirrings to obtain the aluminum

Table 1 Chemical composition of materials (wt%)

	CaO	SiO_2	Al_2O_3	SO_3	Fe_2O_3	MgO	K_2O	TiO_2	Others
Cement	57.61	12.03	5.15	3.46	3.01	1.46	1.21	0.26	15.81
GGBFS	33.83	18.60	15.98	1.01	0.98	7.74	0.39	1.40	20.08
Fly ash	17.58	39.87	28.25	5.07	4.44	1.24	0.70	1.11	1.74

© 2022 The Author(s). Published by the Royal Society of Chemistry

Open Access Article. Published on 13 May 2022. Downloaded on 7/2/2025 11:34:50 PM.
This article is licensed under a Creative Commons Attribution-NonCommercial 3.0 Unported Licence.

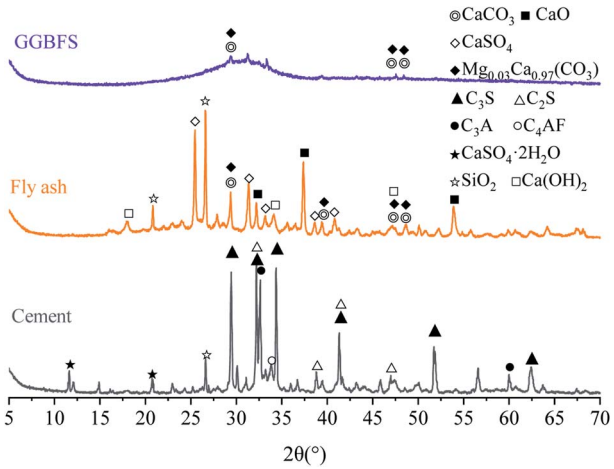

Fig. 1 XRD patterns of cement, fly ash, and GGBFS used in this study.

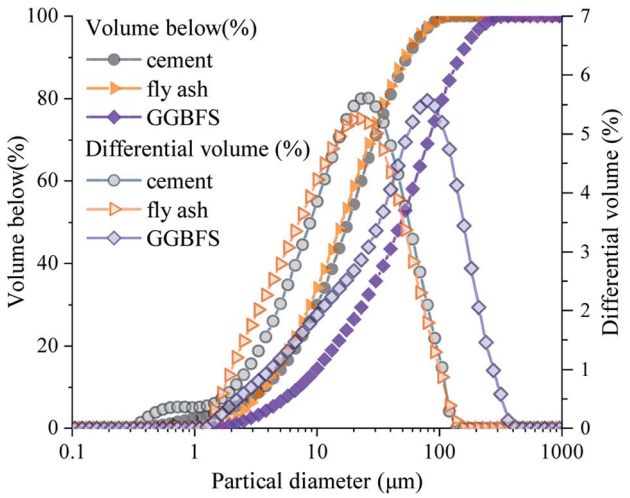

Fig. 2 Particle size distribution of cement, fly ash, and GGBFS.

suspension. Later, all powder materials were dry-mixed in a steel mixing bowl with low-speed stirrings for 2 min, and then the remaining deionized water was poured into the mixing bowl with the same stirrings for another 2 min. These processes yielded sticky cement slurries without a foaming agent. After that, the aluminum suspension was quickly added to the slurries with high-speed stirrings for 30 s, generating homogeneous cement slurries for casting (Fig. 3a). One part of the well-prepared slurries were then poured into disposable paper cups (approximately 100 g each) and covered with plastic wrap (Fig. 3b). The other part of the slurries were poured into a 100 mm cubic mold for compressive strength. In the following 15 min, the concrete "cakes" were inflated by hydrogen gas generated by the reaction between alumina and water. The bubbling process enabled the increases in the volume of cementitious slurries by approximately 80%. The cake-like AC samples were then removed into a standard curing room (20 °C ± 2 °C and 95% RH) for the primary curing for 20 h.

2.3 Carbonation

To facilitate the entry of CO_2 into cement matrix, removal of pore water is recommended.[43–46] Here, a drying scheme of 40 °C for 2 h was used to partially remove the capillary water in the AC specimens before being exposed to CO_2 gas (Fig. 3c).[43–46] This allows for a 7–10% reduction in mass of the AC specimens. The partially dried AC specimens were then moved to a homemade CO_2 curing reactor for carbonation (Fig. 3d).[43] A valve with a digital pressure gage was connected to the reactor to control the gas pressure. Three CO_2 gas pressures, 0.1 bar (0.01 MPa), 1 bar (0.1 MPa), and 2 bar (0.2 MPa), were selected to study the effect of CO_2 pressure on the crystallization of $CaCO_3$ during CO_2 pretreatment. During the entire CO_2 curing period, CO_2 pressure was kept as a preset constant within the variance of ±1 kPa. Owing to the continual consumption of CO_2 by the carbonation of the raw materials and their hydration products, the gas pressure would decrease as carbonation progresses. To save the testing time, the CO_2 curing was stopped when the gas pressure change was less than 1 kPa per 30 min. Results showed that a higher set CO_2 gas pressure reduced the CO_2 curing duration. Specifically, the initial CO_2 gas pressures of 0.1, 1, and 2 bar resulted in curing durations of 8, 5, and 4 h, respectively. Note that the CO_2 curing periods used in this work were significantly shorter than those for the CO_2 curing of ordinary solid concrete at early ages because the porous structure of the AC specimens allowed relatively high gas permeation, thus enhancing the carbonation effect.[42]

2.4 Characterization methods

Samples from the superficial parts of AC specimens were acquired for chemical and microstructure analyses. Particle and powder samples were prepared and dried to a constant weight at 60 °C for different tests. Small AC particles in the size of 10 mm were selected for the SEM test, whereas XRD, FTIR, and TG tests were performed on AC powders that had passed through a 350 mesh sieve. The cube specimens were weighed before and after carbonation, which used as the overall carbon uptake of the block.

SEM was performed using GEMINI 300 ESEM equipped with an energy dispersive spectrometer. A thin layer of gold was sprayed on the freshly fractured surfaces of samples. An accelerating voltage of 3 kV was used.

XRD measurements were performed using a Bruker D8 Advance diffractometer with Cu-Kα radiation ($\lambda = 0.15419$ nm) over a 2θ range of 5° to 90°, and a step length of 0.02°. MDI Jade 6 was used for mineral phase identification.

Table 2 The mixture proportions

	Cement	Fly ash	GGBFS	Water	Aluminum paste	Gypsum
Mass (g)	40	30	30	35	0.5	0.5

© 2022 The Author(s). Published by the Royal Society of Chemistry

Open Access Article. Published on 13 May 2022. Downloaded on 7/2/2025 11:34:50 PM.
This article is licensed under a Creative Commons Attribution-NonCommercial 3.0 Unported Licence.

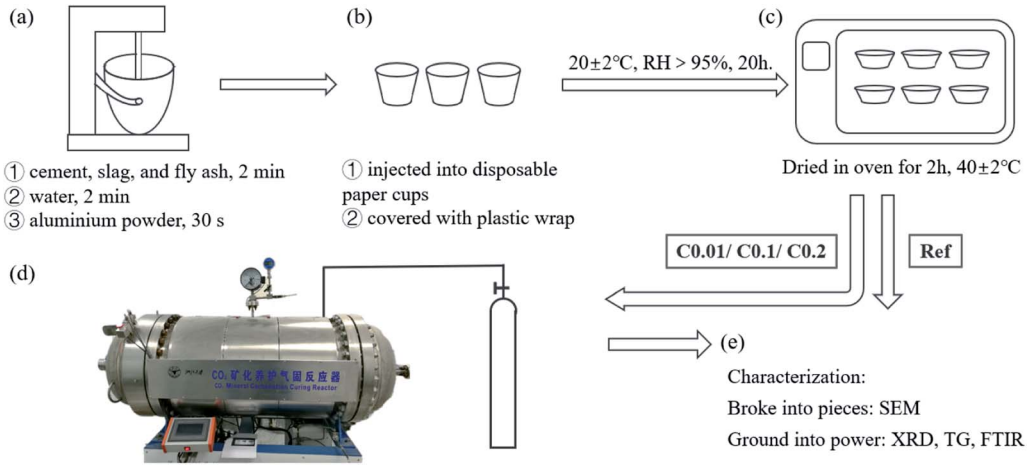

Fig. 3 AC specimen preparation, treatment, and early-age carbonation: (a) cementitious slurries' preparation by mixing and stirring of the raw materials, (b) casting of cementitious slurries, (c) pre-drying of the "cake"-like AC specimens, (d) an *in situ* picture of CO_2 curing reactor, where gas pressure was controlled by the valves during carbonation reactions, (e) characterization methods for the carbonated AC specimens.

FTIR spectra were obtained using an infrared spectrometer AVATAR370. The wavenumber ranges from 4000 to 400 cm^{-1} with a spectral resolution of 4 cm^{-1}, and 32 times of scans were set for all FTIR tests.

TG-DTG texts were conducted using a thermal analyzer TGA2 (Mettler Toledo) in a nitrogen atmosphere. The temperature was increased from 30 °C to 850 °C with a heating rate of 15 °C min^{-1}.

Compressive strength was measured with 100 mm cubic specimens at 3 and 7 days of curing according to Chinese standard GB/T 11971-1997. The compressive strength data were obtained from 4 samples under each type of specimen, and the average values were used for analysis.

3. Results and discussion

3.1 Compressive strength and increased mass

Compressive strength and mass gain of the cube specimens after carbonation are presented in Fig. 4. CO_2 pre-curing resulted in a remarkable increase in the 3d compressive strengths of aerated concrete, from 1.29 MPa of ref specimen to 2.11–2.31 MPa. showing an increase by 164–179%. However, carbonation has some adverse effects on the development of strength, which are positively correlated with the mass gain of the cubes during carbonation. CO_2 pre-curing increases early strength by filling pores with rapidly generated $CaCO_3$ crystals. The adverse effect on strength development stems from the exothermic consumption of water during carbonation, which weakens the subsequent hydration.[19] The high porosity of AC facilitates the entry and transport of CO_2. The porosity of the AC specimens was between 42.20% and 44.42% as measured by X-ray computed tomography and mercury intrusion porosimetry.[42] The mass increase of 100 mm cube samples reached 2.52%, 2.75%, 4.49% under 0.01, 0.1, 0.2 MPa CO_2 curing.

3.2 Chemical outcomes

Hydration of the ternary cement-fly ash-GGBFS system generally generates complex hydration products with complex

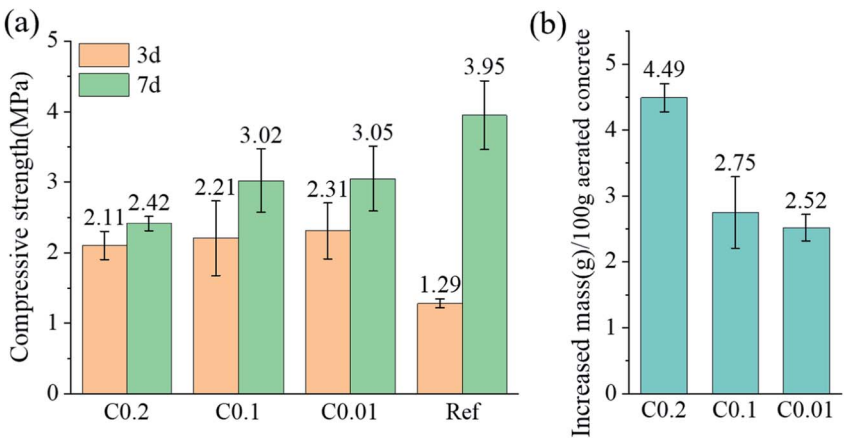

Fig. 4 (a) Compressive strength measured at 3 and 7 days; (b) increased mass of cube specimens after carbonation.

Open Access Article. Published on 13 May 2022. Downloaded on 7/2/2025 11:34:50 PM.
This article is licensed under a Creative Commons Attribution-NonCommercial 3.0 Unported Licence.

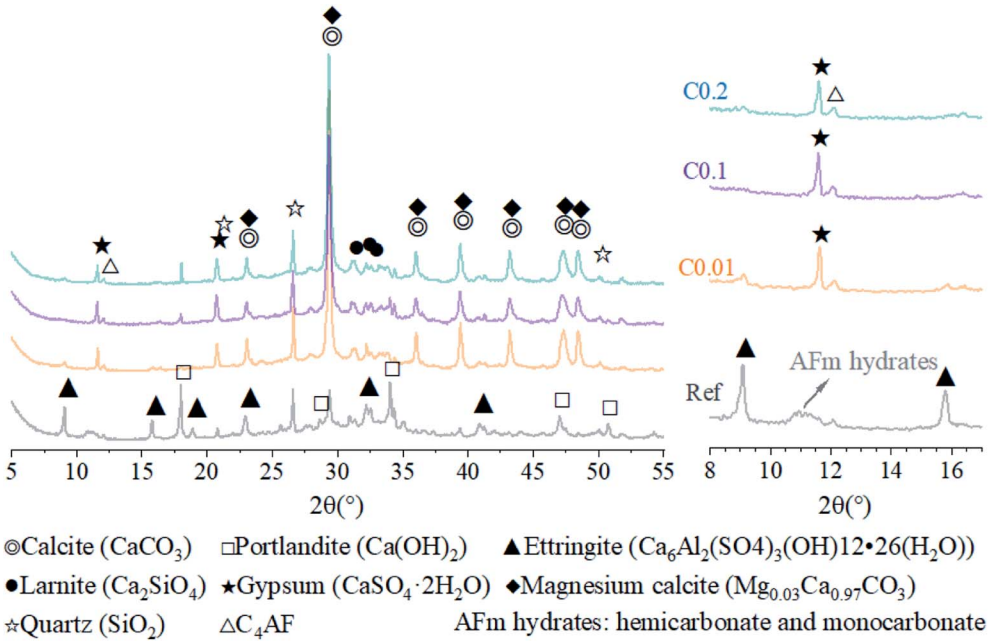

Fig. 5 XRD patterns of AC specimens with and without CO_2 curing within the range of 5° and 55° (left) and the range of 8° and 17° (right).

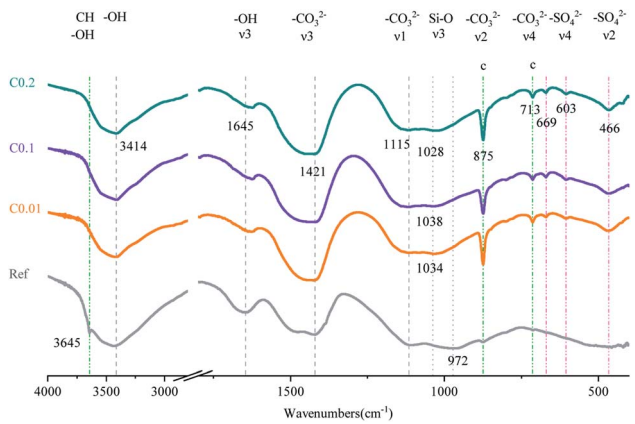

Fig. 6 FTIR spectra of AC specimens with and without CO_2 curing.

microstructures, such as calcium–silicate(aluminum)-hydrate (C–S(A)-H) gel, calcium hydroxide (CH), ettringite (AFt), and mono-sulfoaluminate hydrate (AFm).[47,48] XRD patterns of the reference AC sample in this test suggested the main crystal phases of AFt, CH, quartz, larnite, C_4AF, as well as a small amount of calcite and magnesium calcite (Fig. 5). Among them, quartz, larnite, and magnesium calcite originated from the fly ash and GGBFS (Fig. 1), whereas the remaining crystals were hydration products of the ternary cement–fly ash–GGBFS system. A broad diffraction bump in the 2θ range of 25° to 37° represented the presence of an amorphous phase, *i.e.*, C–S(A)-H, the main hydration products of cement with pozzolanic additives such as fly ash and GGBFS.[49–51]

When the aerated ternary cement-fly ash-GGBFS specimens were exposed to environments with relatively high CO_2 gas pressures, carbonation began to occur for the active phases in the hydration products and raw materials. For simplification, only phases with obvious mass changes (*e.g.*, CH, AFt, C–S(A)-H) were representatively selected to demonstrate the carbonation processes, which can be given by:[10,52]

$$Ca(OH)_2 + CO_2 \rightarrow CaCO_3 + H_2O \quad (1)$$

$$3CaO·Al_2O_3·3CaSO_4·32H_2O + 3CO_2 \rightarrow 3CaCO_3 + 3CaSO_4·2H_2O + Al_2O_3 + 26H_2O \quad (2)$$

$$xCaO·SiO_2·yAl_2O_3·zH_2O + xCO_2 \rightarrow xCaCO_3 + SiO_2 + yAl_2O_3 + zH_2O \quad (3)$$

For the carbonation of CH, in the FTIR curves (Fig. 6), the peak near 3645 cm^{-1} ascribed to O–H stretching in CH[53] was observed only in the Ref sample, evidencing the generation of CH in the Ref AC sample due to cement hydration and the vanishing of CH in the carbonated samples due to the carbonation reaction. However, both XRD and TGA spectra continued showing the characteristic peaks of CH after the early-age carbonation (Fig. 5 and 7), suggesting the incomplete CH carbonation. Taking the TGA data for example (Fig. 6d), the weight loss peak near 450 °C, corresponding to the dehydroxylation of CH,[54] was 0.4%, 0.56%, and 0.66% for the AC samples of C0.01, C0.1, and C0.2, respectively, compared with 1.51% for the Ref AC sample. The small difference in the amount of residual CH after carbonation may be due to the different reaction rates and times under different CO_2 pressures. A longer CO_2 curing time at a lower pressure may result in a greater degree of CH carbonation. Moreover, the exothermic nature of cement carbonation may raise the temperature and, consequently, reduce the solubility of CH in water, resulting in less CH being carbonated at a higher CO_2 gas pressure (Fig. 5 and 7d).

© 2022 The Author(s). Published by the Royal Society of Chemistry

Open Access Article. Published on 13 May 2022. Downloaded on 7/2/2025 11:34:50 PM.
This article is licensed under a Creative Commons Attribution-NonCommercial 3.0 Unported Licence.

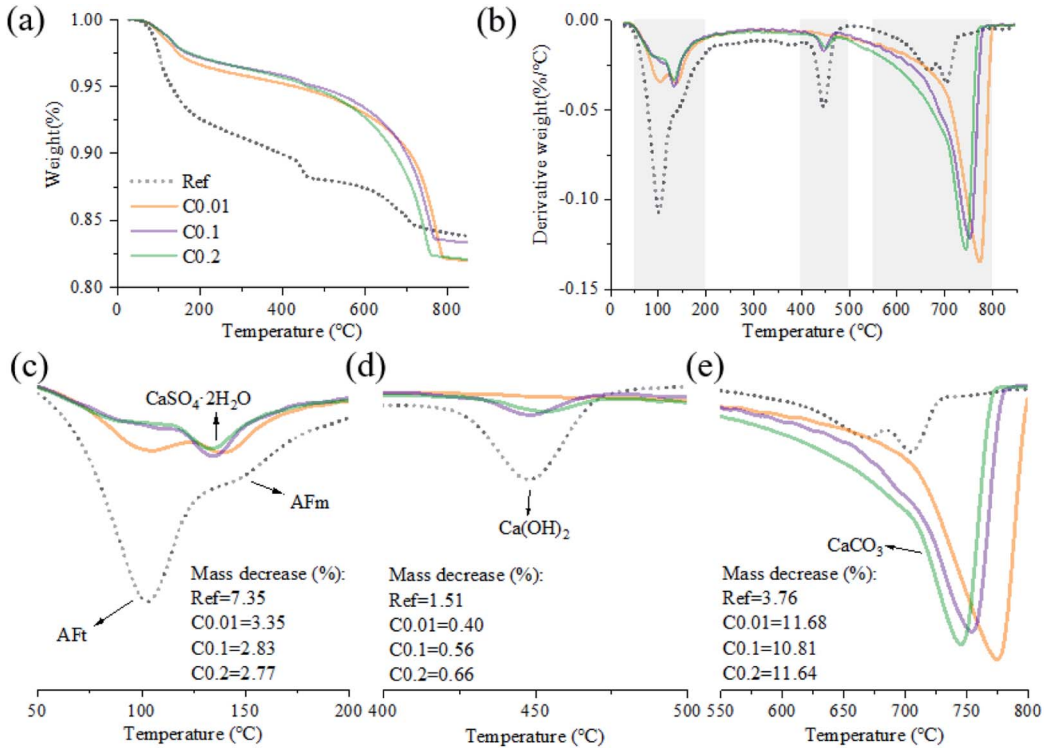

Fig. 7 TG-DTG curves of the AC specimens cured by different CO_2 pressures: (a) TG and (b) DTG curves over the entire testing temperature range; (c) DTG curves between 50 °C and 200 °C showing the characteristic peaks related to the removal of strongly confined water and the dehydration of AFt, AFm, and gypsum; (d) those between 400 °C and 500 °C showing the characteristic peaks related to the decomposition of CH; (e) those between 550 °C and 800 °C showing the characteristic peaks related to the decomposition of $CaCO_3$.

Regarding the carbonation of AFt, its XRD characteristic peaks almost disappeared, whereas those of gypsum became greatly significant according to the reaction (2). The small bump between 10.5° and 11.5° (Fig. 5), representing the poorly crystalline AFm hydrates,[55] became flat and enhanced the characteristic peaks of gypsum after carbonation. Slight peaks ranging from 466 to 669 cm^{-1} in the FTIR spectra (Fig. 6) indicated the generation of gypsum due to the carbonation of AFt and AFm. The SO_4^{2-} symmetry bending vibration peak (ν2) in gypsum appeared at 464 cm^{-1}, and the SO_4^{2-} antisymmetric bending vibration peak (ν4) appeared at 603 and 670 cm^{-1}.[56] The DTG spectra (Fig. 7c) showed similar results. The mass loss below 200 °C was caused by the removal of strongly adsorbed water (*i.e.*, water confined between C–S(A)-H layers) and the dehydration of crystals (*i.e.*, AFt, AFm, and gypsum) (Fig. 7c). Specifically, the peaks at 110 °C, 130 °C, and 150 °C denoted the decomposition of AFt, gypsum, and AFm, respectively.[57,58] The mass loss of the Ref. AC sample below 200 °C was 7.35%, and those of the carbonized samples were heavily decreased to 2.77–3.35%. For the C0.01 sample, a slight AFt peak at 110 °C still existed, suggesting incomplete carbonation of AFt at the low CO_2 gas pressure. This finding agreed with the XRD spectra of the C0.01 sample, where the characteristic peaks of AFt continued to be observed (Fig. 5).

For the carbonation of C–S(A)-H gel, which is generally not a bulk crystalline phase, it would be difficult to obtain meaningful findings from the XRD spectra of the Ref. AC sample (Fig. 5). However, some C–S(A)-H gel features may be characterized by FTIR. In Fig. 3, the asymmetrical stretching vibration (ν_3) of the Si–O bond between 800 and 1200 cm^{-1} was the main feature of C–S(A)-H.[59] The turning point of the curves shifted from 972 cm^{-1} to 1028–1038 cm^{-1} after carbonation, implying the transmission of the silicate network from Q2 units to Q3 units. This suggested that after carbonation, the C–S(A)-H chain

Table 3 Mass decrease in each temperature range measured by TG

Temperature range (°C)	Mass decrease (%)				Minerals and/or confined water
	Ref.	C0.01	C0.1	C0.2	
50–200	7.35	3.35	2.83	2.77	AFt, AFm, $CaSO_4 \cdot 2H_2O$, confined water
400–500	1.51	0.4	0.56	0.66	$Ca(OH)_2$
550–800	3.76	11.68	10.81	11.64	$CaCO_3$

Open Access Article. Published on 13 May 2022. Downloaded on 7/2/2025 11:34:50 PM.
This article is licensed under a Creative Commons Attribution-NonCommercial 3.0 Unported Licence.

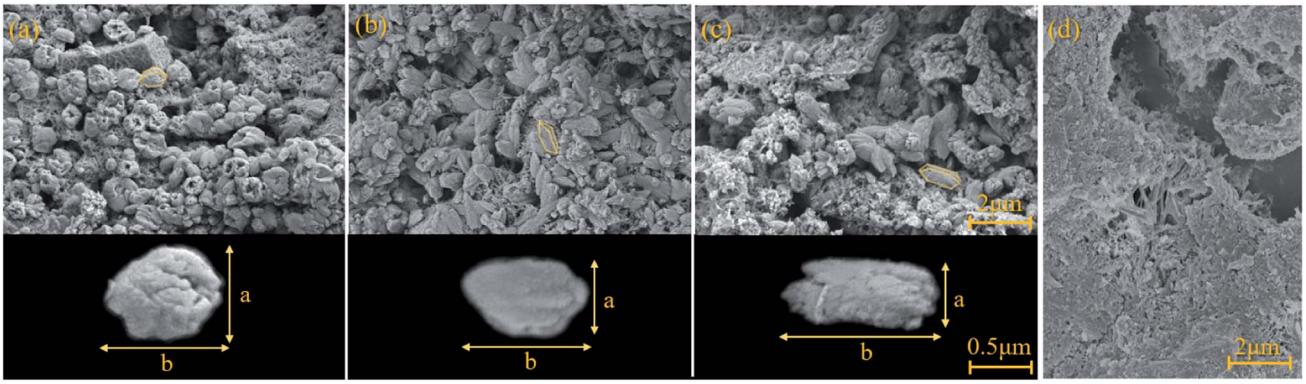

Fig. 8 Selected SEM images of AC samples under different curing pressures (a: C0.01; b: C0.1; c: C0.2) (top) and magnified $CaCO_3$ particles (bottom); (d) SEM pictures of Ref samples within a similar location.

shrank and the non-bridging oxygen on the silicate sites decreased.[36,60–62]

Then, the mineral characteristics of $CaCO_3$ (Fig. 5–7) were investigated. According to the XRD results, only calcite and magnesium calcite were identified (Fig. 5). The magnesium calcite may be derived from the carbonation of magnesium oxide in GGBFS, where magnesium replaced the trace calcium.

According to the FTIR tests, the characteristic bands of $-CO_3^{2-}$ were identified in the range of ν1 (symmetric C–O stretching) around 1100 cm^{-1}, ν2 ($-CO_3$ out-of-plane bending) around 875 cm^{-1}, ν3 (asymmetric $-CO_3$) around 1420 cm^{-1}, and ν4 (doubly degenerated in-plane O–C–O deformation bending) around 713 cm^{-1}.[30,63] The C–O stretching ν2 and ν4 modes characterized the products of CO_2 treatment. Three polymorphs of $CaCO_3$ exhibit distinct peaks in these two ranges. Only the characteristic peaks of calcite (875 (ν2) and 713 (ν4) cm^{-1}) were observed, whereas the peaks of aragonite (ν2 region (854 and 843 cm^{-1}) and ν4 region (712 and 700 cm^{-1}) and vaterite (873 (ν2) and 744 (ν4) cm^{-1}) did not appear.[36,64]

TGA tests can quantify the decomposition of $CaCO_3$.[65] Here, the mass loss between 550 °C and 800 °C was adopted to evaluate the amount of $CaCO_3$ (Fig. 7e).[65] In Table 3, the mass decrease in each temperature range was calculated, and the major related minerals and/or confined water were indicated. The $CaCO_3$ produced by carbonation was derived from $Ca(OH)_2$, AFt, AFm and C–S(A)-H gel. The mass loss of AC specimens pre-cured at the CO_2 pressures of 0.1, 1, and 2 bar was nearly the same, *i.e.*, 11.68%, 10.81%, and 11.64%, respectively (Fig. 7e). It is equivalent to the sorption rate of 35 g CO_2 per 100 g cement. The mass loss of the Ref. AC sample between 550 °C and 800 °C was 3.76%, indicating the presence of $CaCO_3$, which could be partially derived from raw materials (fly ash and GGBFS) and from the natural carbonation of the Ref. AC sample in the atmosphere. The characteristic DTG peak of $CaCO_3$ decomposition may be related to the degree of crystallization.[66,67] According to this regime, $CaCO_3$ produced by a sample cured with a lower pressure and a longer duration would show a better degree of crystallinity based on the tests (Fig. 7e).

3.3 Calcium carbonate crystal morphology

Fig. 8 representatively displays the selected SEM pictures of the fresh fracture surface of the AC specimens on a microscale. In the CO_2 cured samples, some calcite crystals were discovered on the newly fractured surface. The crystalline morphology of calcite may vary in different carbonation conditions. For example, cubes, prisms, spherical aggregates, and other irregular shapes of calcite have been observed.[35] Compared with well-crystallized calcite that nucleates and grows in dilute hydrated cement,[39] the observed $CaCO_3$ crystals in carbonized CBMs were mostly granular and clustered together.[24,41,68–70] The rhombohedral crystal structure is a typical equilibrium form of calcite, which is typically precipitated from a homogeneous solution, whereas the process of industrial CO_2 gas carbonation typically forms scalenohedral calcite.[71–73] The scalenohedral calcite crystals observed in this experiment were scattered in the pores of the AC material, showing irregular shapes and layered accumulations (Fig. 8). The crystals were stacked in a loosely packed structure, yielding rough surfaces. In specification, the low-pressure cured sample exhibited hollow dents at both ends of the crystal (Fig. 8a), which may be caused by the excessive growth of edges of the crystal at both ends.[74]

In addition, the complexity of the raw materials has significant impacts on the crystal morphology and microstructure of carbonated materials. For example, the presence of Mg, K, and SO_3 in the raw materials of cement and fillers may impact the crystallization of calcite during carbonation. It was suggested that the electron configuration of Mg^{2+}can delay the growth of calcium carbonation in its vicinity,[75,76] resulting in rougher terraces and rounded steps.[77] The carbonation of calcium with $MgSO_4$ will form polycrystalline aggregates, small and irregular pits, and rugged terrace edges due to the inhibition of carbonation caused by SO_4^{2-}.[78] The presence of K ions may control the crystal morphology of $CaCO_3$, stabilizing the rhombic face on rhombohedral calcite crystals.[74]

As CO_2 curing pressure increases, the $CaCO_3$ crystals change their appearance but still maintain the rhombohedral structure. Geometrical characteristics of the crystal particles were measured to quantify the morphological changes of $CaCO_3$ crystals, *i.e.*, the long-axis length, *b*, the short-axis length (or

© 2022 The Author(s). Published by the Royal Society of Chemistry

Open Access Article. Published on 13 May 2022. Downloaded on 7/2/2025 11:34:50 PM.
This article is licensed under a Creative Commons Attribution-NonCommercial 3.0 Unported Licence.

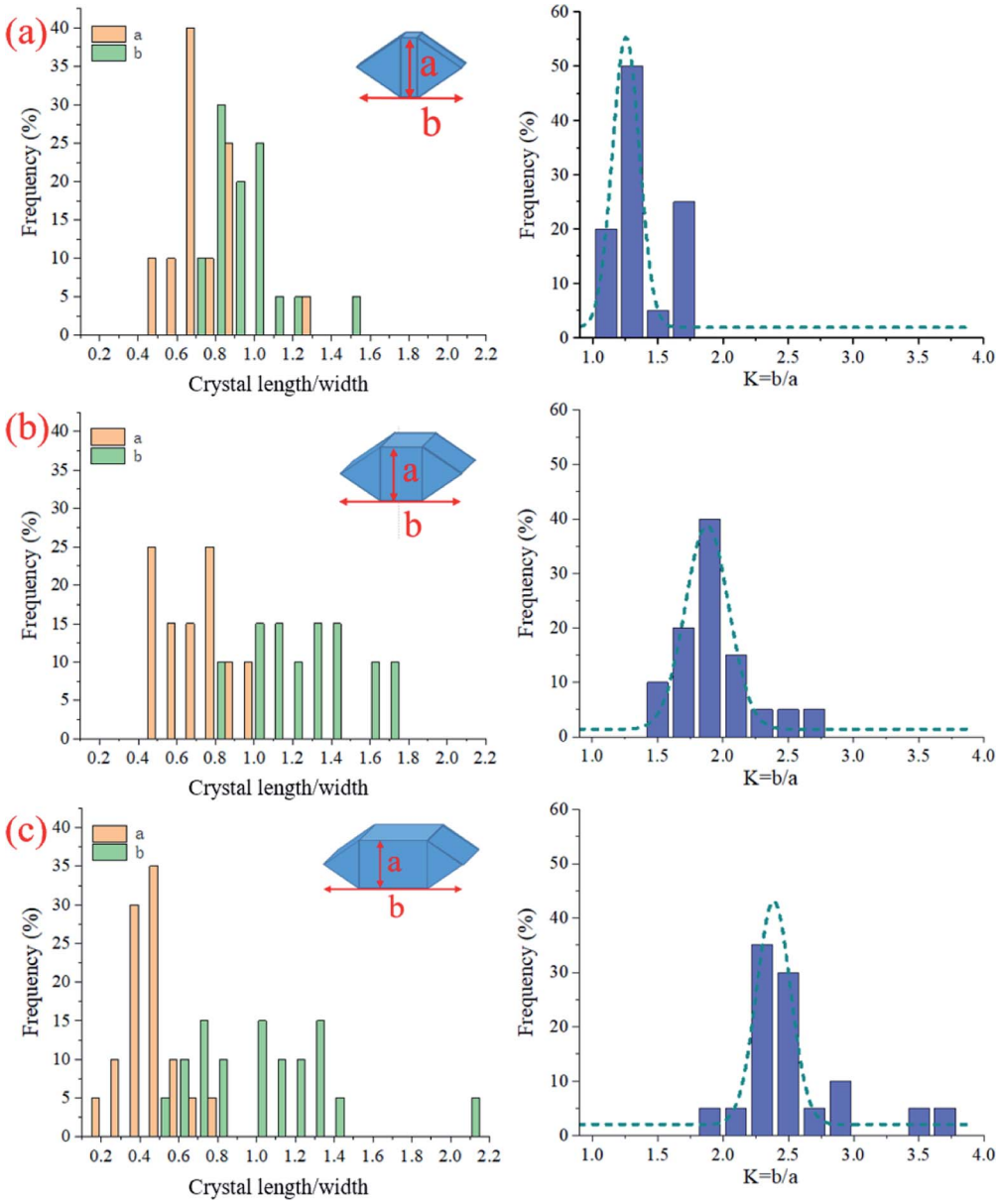

Fig. 9 Statistics data of $CaCO_3$ crystal length, width, and the aspect ratio for the AC specimens cured at different CO_2 pressures: (a) C0.01, (b) C0.1, and (c) C0.2.

width), *a*, and the length/width ratio (or aspect ratio), *K*; see the bottom half of Fig. 8. Only particles whose shape can be observed were selected, and at least 20 $CaCO_3$ particles of each sample were statistically analyzed.

Fig. 9 shows the acquired morphological parameters (*a*, *b*, *K*) of the selected $CaCO_3$ crystals. At the low CO_2 gas pressure (0.1 bar), the crystals' length was slightly higher than the width, and both were distributed near 1 μm (Fig. 9a). At the higher CO_2 gas pressures (1 and 2 bar), the length was unchanged in the range of 0.8–1.8 μm, but the width decreased significantly from 0.6 μm to 0.4 μm (Fig. 9b and c). As a result, the aspect ratio K increased from 1.3 ± 0.19 to 2.5 ± 0.44 when CO_2 gas pressure increased from 0.1 to 2 bar; see the left panel of Fig. 9.

In this experiment, the *K* value increased linearly with CO_2 pressure, with a linear fitting determination coefficient greater than 0.999 (Fig. 10). Changes in the morphology of $CaCO_3$ crystals with CO_2 pressure were also observed in the literature.[16,24,41,68,70] Here, the aspect ratio of $CaCO_3$ crystals was obtained by measuring the geometric parameters based on the reported SEM images. As shown in Fig. 10, the aspect ratios of $CaCO_3$ crystals in the literature showed a similar to the result, that is, a higher CO_2 pressure can lead to a higher aspect ratio.

3.4 Discussion of mechanisms

The experiments demonstrated that unlike the well-crystallized calcite after carbonation in a dilute hydrated cement system, $CaCO_3$ crystals in AC specimens showed different

Open Access Article. Published on 13 May 2022. Downloaded on 7/2/2025 11:34:50 PM.
This article is licensed under a Creative Commons Attribution-NonCommercial 3.0 Unported Licence.

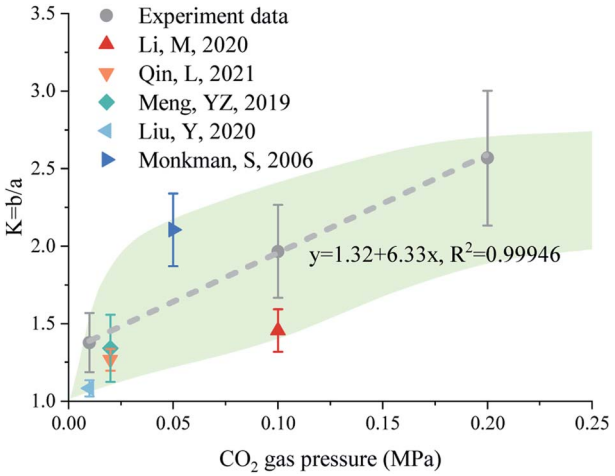

Fig. 10 The statistic K (length-to-width ratio) of $CaCO_3$ crystals measured in this work and reported in the literature.[26,32,40,69,71]

morphological characteristics (Fig. 8–10). Specifically, a hollow structure was observed for $CaCO_3$ crystals in the AC sample cured at 0.1 bar CO_2 (Fig. 7a), and as the gas pressure was increased to 2 bar, this hollow structure gradually disappeared and the aspect ratio increased (Fig. 9). The changes in $CaCO_3$ crystal structure are associated with crystallization processes, which are highly dependent on carbonation environments. Suzuki *et al.*[79] observed polycrystalline calcite with a hollow structure and confirmed that this hollow structure may originate from the transformation of crystals from vaterite or ACC solid to calcite. Compared with calcite, ACC contains 1.0–1.5 water molecules per $CaCO_3$ unit,[80] and the density of vaterite is lighter in weight by 6.3%. This solid-to-solid transformation was accompanied by the release of water and volume reduction, thereby forming cavities.[79]

Two gas pressure-dependent crystallization paths were proposed to better demonstrate the effect of gas pressure on the morphology of $CaCO_3$ crystals (Fig. 11). At the beginning stage of CBMs' carbonation, cement and cement hydration products

Table 4 Corresponding CO_2 solubility under different CO_2 curing pressure

Sample	CO_2 pressure (Mpa)	CO_2 solubility (mol L^{-1})
C0.01	0.01	0.0037
C0.1	0.1	0.0365
C0.2	0.2	0.0730

released Ca^{2+}, OH^- and H_4SiO_4 in the pore solution[81] and CO_2 dissolved in the pore solution to release CO_3^{2-}.[81] The corresponding CO_2 solubility under different CO_2 curing pressures was listed (Table 4). At the gas pressure of 0.01, 0.1 and 0.2 MPa, the ideally dissolved CO_2 concentrations were 0.0037, 0.0365 and 0.0730 mol L^{-1}. The combination of Ca^{2+} and CO_3^{2-} under oversaturated conditions could form critical-size clusters that subsequently form ACC nanoparticles covering the surfaces of the substrate, a process known as crystal nucleation[82] (Fig. 11). At this stage, ACC nanoparticles are still unstable, and the paths to crystals are highly dependent on the supplies of Ca^{2+} and CO_3^{2-}, as well as other impacting factors. At a low CO_2 gas pressure (*e.g.*, 0.1 bar), ACC nanoparticles gradually aggregated and formed spherical vaterite and then slowly transformed into calcite with cavities;[78] see the low-pressure path shown in Fig. 10. When CO_2 gas pressure was increased (*e.g.*, 2 bar), the slender calcite, composed of scalenohedron, was formed from ACC nanoparticles at a faster rate; see the high pressure path shown in Fig. 11. In addition, high CO_2 pressures may induce the formation of elongated crystal aggregates. Excessive carbonate ions can hinder the growth of the surface of the calcite crystal in the minor axis direction, causing the crystal to grow to the tips of both ends.[83] The crystals in samples with lower K values may have better thermodynamic stability, so the characteristic decomposition temperature is higher (Fig. 7e).

Overall, the experimental work reported different morphological characteristics of $CaCO_3$ formed under different CO_2 pressures (Fig. 8–10), whereas the total carbonation degrees had no great differences (Fig. 7). The findings would uncover the

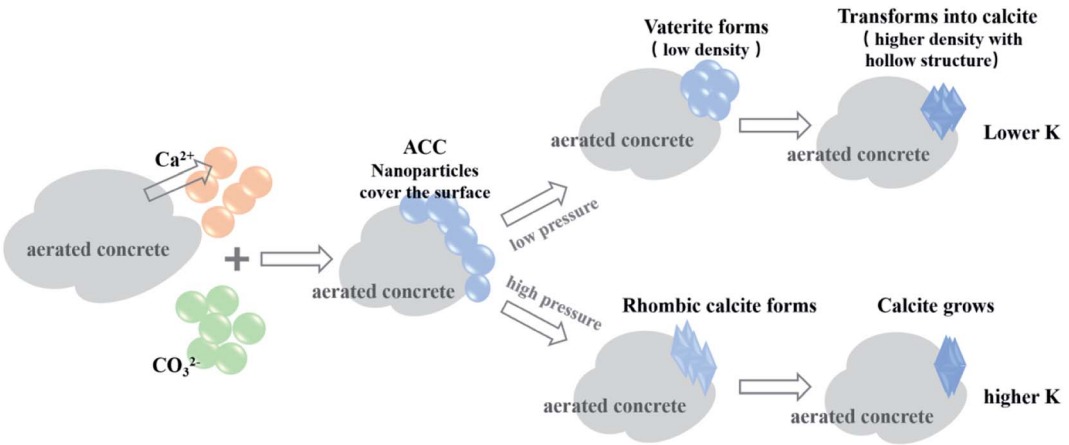

Fig. 11 Schematic illustration of the crystal growth paths of $CaCO_3$ to form crystals with low and high aspect ratio K at different CO_2 pressures.

© 2022 The Author(s). Published by the Royal Society of Chemistry

Open Access Article. Published on 13 May 2022. Downloaded on 7/2/2025 11:34:50 PM. This article is licensed under a Creative Commons Attribution-NonCommercial 3.0 Unported Licence.

physicochemical mechanisms of carbonation of CBMs affected by CO_2 pressure. Further rigorous work is required to establish paths to design and control carbonation conditions, which enable optimizing engineering performance and CO_2 sinking efficacy of CBMs.

4. Conclusion

(1) In AC, components participating in carbonation include CH, AFt, AFm, and C–S(A)-H gel. After C–S(A)-H gel was carbonized, the silicate network transformed from Q2 units into Q3 units, and the C–S(A)-H chain shrunk. Under the CO_2 pressures of 0.01–0.2 MPa, the amount of $CaCO_3$ was detected as 10.81–11.68%. $CaCO_3$ formed under a lower pressure showed a higher decomposition temperature and a better degree of crystallinity.

(2) The crystalline products after the carbonation of AC were calcite and gypsum, which were dispersed in the matrix rather than being closely packed. When AC samples were cured at low pressure, the final product calcite, whose width and length were distributed near 1 μm, had a smaller K value ($K = 1.3 \pm 0.19$). When high pressure was used, the calcite, whose width was approximately 0.4 μm and length ranged from 0.6 to 1.4 μm, had an increased K value ($K = 2.5 \pm 0.44$).

(3) The influence of CO_2 pressure on the morphology of $CaCO_3$ crystals originated from different crystallization paths. Under low CO_2 pressure, ACC nanoparticles gradually aggregated and formed spherical vaterite and then slowly transformed into calcite with the cavity through a solid–solid phase change. Under high CO_2 gas pressure, ACC nanoparticles rapidly formed slender calcites composed of scalenohedrons.

(4) The experiments uncovered the different morphological characteristics of $CaCO_3$ crystals in early-age carbonated concrete as well as the mechanisms of carbonation parts in different CO_2 pressures. The findings would clarify the mechanisms to control crystallization patterns with rational design and manipulation of materials ' microstructure for better CO_2 utilizations.

Author contributions

Jiayu Lu: conceptualization, investigation, formal analysis & original draft. Shengqian Ruan: investigation, review & editing. Yi Liu: supervision, review & editing. Tao Wang: supervision. Qiang Zeng: conceptualization, supervision, review & editing. Dongming Yan: supervision, review & editing. The manuscript was written through contributions of all authors. All authors have given approval to the final version of the manuscript.

Conflicts of interest

There are no conflicts of interest to declare.

Acknowledgements

The authors acknowledge the financial supports from the National Natural Science Foundation of China (No. 52171277, 51878602, and 52038004).

References

1 C. B. M. Federation, *Carbon Emission Report of China's Building Materials Industry*, 2020, **http://www.cbmf.org/cbmf/yw/7063198/index.html**, (accessed 26 September 2021).
2 *Analysis of Cement Industry Carbon Emission Status and Discussion on Critical Paths of Emission Reduction*, **http://www.cbmd.cn/actrice/10545.html**, accessed accessed 26 September 2021.
3 Q. Li, L. Zhang, X. Gao and J. Zhang, *Constr. Build. Mater.*, 2020, **230**, 116990.
4 P. He, C. S. Poon and D. C. W. Tsang, *Cem. Concr. Compos.*, 2018, **86**, 98–109.
5 Z. Tu, C. Shi and N. Farzadnia, *J. Mater. Civ. Eng.*, 2018, **30**, 04018164.
6 T. Chen, M. Bai and X. Gao, *J. CO2 Util.*, 2021, **51**, 101633.
7 X. Li and T. Ling, *J. CO2 Util.*, 2020, **38**, 348–354.
8 L. Wang, L. Chen, D. C. W. Tsang, B. Guo, J. Yang, Z. Shen, D. Hou, Y. S. Ok and C. S. Poon, *J. Cleaner Prod.*, 2020, **258**, 120678.
9 H. Mehdizadeh, Y. Meng, M. Guo and T. Ling, *Constr. Build. Mater.*, 2021, **289**, 123193.
10 D. Sharma and S. Goyal, *J. Cleaner Prod.*, 2018, **192**, 844–854.
11 S. K. Kaliyavaradhan, T. Ling and K. H. Mo, *J. CO2 Util.*, 2020, **42**, 101330.
12 T. Chen and X. Gao, *ACS Sustainable Chem. Eng.*, 2020, **8**, 3872–3884.
13 B. Liu, J. Qin, J. Shi, J. Jiang, X. Wu and Z. He, *Constr. Build. Mater.*, 2021, **272**, 121660.
14 A. Smigelskyte and R. Siauciunas, *J. Therm. Anal. Calorim.*, 2019, **138**, 2651–2659.
15 D. Xuan, B. Zhan, C. S. Poon and W. Zheng, *Constr. Build. Mater.*, 2016, **113**, 664–672.
16 S. Monkman and Y. Shao, *J. Mater. Civ. Eng.*, 2006, **18**, 768–776.
17 D. Zhang, Z. Ghouleh and Y. Shao, *J. CO2 Util.*, 2017, **21**, 119–131.
18 B. Song, C. Shi, X. Hu, K. Ouyang, Y. Ding and G. Ke, *Constr. Build. Mater.*, 2021, **288**, 123113.
19 L. Qin, X. Gao and T. Chen, *Constr. Build. Mater.*, 2019, **212**, 653–662.
20 Y. Wang, S. Liu, L. Zhang, M. Gan, X. Miao, N. Wei, X. Cheng, H. Liu, X. Li and J. Li, *Appl. Geochem.*, 2021, **128**, 104937.
21 V. Rostami, Y. Shao and A. J. Boyd, *J. Mater. Civ. Eng.*, 2012, **24**, 1221–1229.
22 D. Zhang and Y. Shao, *Constr. Build. Mater.*, 2016, **123**, 516–526.
23 M. R. Cabral, E. Y. Nakanishi and J. Fiorelli, *J. Mater. Civ. Eng.*, 2017, **29**, 04017018.
24 L. Qin, X. Gao, A. Su and Q. Li, *J. Cleaner Prod.*, 2021, **278**, 123897.
25 D. Zhang and Y. Shao, *J. CO2 Util.*, 2018, **27**, 137–144.
26 X. Zhong, L. Li, Y. Jiang and T. Ling, *Constr. Build. Mater.*, 2021, **302**, 124158.
27 C. Shi and Y. Wu, *Resour., Conserv. Recycl.*, 2008, **52**, 1087–1092.

© 2022 The Author(s). Published by the Royal Society of Chemistry

Open Access Article. Published on 13 May 2022. Downloaded on 7/2/2025 11:34:50 PM. This article is licensed under a Creative Commons Attribution-NonCommercial 3.0 Unported Licence.

28 B. Kottititum, T. P. Quoc, N. Maes, W. Prakaypan and T. Srinophakun, *Appl. Sci.*, 2018, **8**, 190.
29 Z. Tu, M. Guo, C. S. Poon and C. Shi, *Cem. Concr. Compos.*, 2016, **72**, 9–16.
30 A. Hidalgo, C. Domingo, C. Garcia, S. Petit, C. Andrade and C. Alonso, *J. Mater. Sci.*, 2008, **43**, 3101–3111.
31 Y. Li, W. Liu, F. Xing, S. Wang, L. Tang, S. Lin and Z. Dong, *J. CO2 Util.*, 2020, **35**, 303–313.
32 Y. Mu, Z. Liu and F. Wang, *ACS Sustainable Chem. Eng.*, 2019, **7**, 7058–7070.
33 X. Ke, M. Criado, J. L. Provis and S. A. Bernal, *ACS Sustainable Chem. Eng.*, 2018, **6**, 5067–5075.
34 A. Morandeau, M. Thiery and P. Dangla, *Cem. Concr. Res.*, 2014, **56**, 153–170.
35 G. Falini, S. Fermani, M. Goisis and G. Manganelli, *Cryst. Growth Des.*, 2009, **9**, 2240–2247.
36 H. Mehdizadeh, X. Jia, K. H. Mo and T. Ling, *Environ. Pollut.*, 2021, **280**, 116914.
37 Z. Yi, T. Wang and R. Guo, *J. CO2 Util.*, 2020, **40**, 101196.
38 G. Falini, S. Manara, S. Fermani, N. Roveri, M. Goisis, G. Manganelli and L. Cassar, *Crystengcomm*, 2007, **9**, 1162–1170.
39 J. Jiang, Q. Zheng, D. Hou, Y. Yan, H. Chen, W. She, S. Wu, D. Guo and W. Sun, *Phys. Chem. Chem. Phys.*, 2018, **20**, 14174–14181.
40 R. Siauciunas, H. Hilbig, E. Prichockiene, A. Smigelskyte and Z. Takulinskas, *Ceram. Int.*, 2020, **46**, 29436–29442.
41 M. Li, Q. Wang, J. Yang, X. Guo and W. Zhou, *Ksce J. Civ. Eng.*, 2021, **25**, 805–821.
42 D. Yan, J. Lu, Y. Sun, T. Wang, T. Meng, Q. Zeng and Y. Liu, *ACS Sustainable Chem. Eng.*, 2021, **9**, 3363–3375.
43 S. Praneeth, R. Guo, T. Wang, B. K. Dubey and A. K. Sarmah, *Constr. Build. Mater.*, 2020, **244**, 118363.
44 D. Zhang, V. C. Li and B. R. Ellis, *ACS Sustainable Chem. Eng.*, 2019, **7**, 16310–16319.
45 D. Zhang, V. C. Li and B. R. Ellis, *ACS Sustainable Chem. Eng.*, 2018, **6**, 15976–15981.
46 I. Mehdipour, G. Falzone, E. C. La Plante, D. Simonetti, N. Neithalath and G. Sant, *ACS Sustainable Chem. Eng.*, 2019, **7**, 13053–13061.
47 K. L. Scrivener and A. Nonat, *Cem. Concr. Res.*, 2011, **41**, 651–665.
48 S. A. Yaseen, G. A. Yiseen and Z. Li, *ACS Omega*, 2019, **4**, 10160–10170.
49 B. G. Kutchko, B. R. Strazisar, G. V. Lowry, D. A. Dzombak and N. Thaulow, *Environ. Sci. Technol.*, 2008, **42**, 6237–6242.
50 M. Zhang and S. Bachu, *Int. J. Greenhouse Gas Control*, 2011, **5**, 826–840.
51 E. A. C. Panduro, M. Torsaeter, K. Gawel, R. Bjorge, A. Gibaud, A. Bonnin, C. M. Schlepuetz and D. W. Breiby, *Cryst. Growth Des.*, 2019, **19**, 5850–5857.
52 V. G. Papadakis, C. G. Vayenas and M. N. Fardis, *ACI Mater. J.*, 1991, **88**, 363–373.
53 C. Rodriguez-Navarro, K. Elert and R. Sevcik, *CrystEngComm*, 2016, **18**, 6594–6607.
54 M. R. Cabral, E. Y. Nakanishi, V. Dos Santos, C. Gauss, S. F. Dos Santos and J. Fiorelli, *Mater. Struct.*, 2018, **51**, 52.
55 J. Skocek, M. Zajac and M. Ben Haha, *Sci. Rep.*, 2020, **10**, 5614.
56 D. Zhang, Z. Yuan, S. Wang, Y. Jia and G. P. Demopoulos, *J. Hazard. Mater.*, 2015, **300**, 272–280.
57 M. Boumaaza, B. Huet, P. Turcry and A. Ait-Mokhtar, *Cem. Concr. Res.*, 2020, **135**, 106113.
58 D. Gastaldi, F. Bertola, F. Canonico, L. Buzzi, S. Mutke, S. Irico, G. Paul, L. Marchese and E. Boccaleri, *Cem. Concr. Res.*, 2018, **109**, 30–41.
59 M. Thiery, G. Villain, P. Dangla and G. Platret, *Cem. Concr. Res.*, 2007, **37**, 1047–1058.
60 R. Ylmen, L. Wadso and I. Panas, *Cem. Concr. Res.*, 2010, **40**, 1541–1546.
61 W. Ashraf and J. Olek, *J. Mater. Sci.*, 2016, **51**, 6173–6191.
62 Y. Shao, V. Rostami, Z. He and A. J. Boyd, *J. Mater. Civ. Eng.*, 2014, **26**, 117–124.
63 E. E. Coleyshaw, G. Crump and W. P. Griffith, *Spectrochim. Acta, Part A*, 2003, **59**, 2231–2239.
64 R. Chang, D. Choi, M. H. Kim and Y. Park, *ACS Sustainable Chem. Eng.*, 2017, **5**, 1659–1667.
65 X. Pan, C. Shi, N. Farzadnia, X. Hu and J. Zheng, *Cem. Concr. Compos.*, 2019, **99**, 89–99.
66 G. Villain, M. Thiery and G. Platret, *Cem. Concr. Res.*, 2007, **37**, 1182–1192.
67 T. Chen and X. Gao, *J. CO2 Util.*, 2019, **34**, 74–86.
68 Y. Meng, T. Ling, K. H. Mo and W. Tian, *Sci. Total Environ.*, 2019, **671**, 827–837.
69 S. Ahmad, R. A. Assaggaf, M. Maslehuddin, O. S. Baghabra Al-Amoudi, S. K. Adekunle and S. I. Ali, *Constr. Build. Mater.*, 2017, **136**, 565–573.
70 Y. Liu, Z. Yan, C. W. K. Chow, A. Keegan, N. P. Phuong, D. Li, G. Qian and L. Wang, *Sci. Total Environ.*, 2020, **746**, 141182.
71 D. Aquilano, M. Bruno, F. R. Massaro and M. Rubbo, *Cryst. Growth Des.*, 2011, **11**, 3985–3993.
72 R. Beck and J. Andreassen, *J. Cryst. Growth*, 2010, **312**, 2226–2238.
73 A. M. Lopez-Periago, R. Pacciani, L. F. Vega and C. Domingo, *Cryst. Growth Des.*, 2011, **11**, 5324–5332.
74 G. Falini, S. Fermani, G. Tosi and E. Dinelli, *Cryst. Growth Des.*, 2009, **9**, 2065–2072.
75 D. Di Tommaso and N. H. de Leeuw, *Phys. Chem. Chem. Phys.*, 2010, **12**, 894–901.
76 S. Kerisit and S. C. Parker, *J. Am. Chem. Soc.*, 2004, **126**, 10152–10161.
77 M. R. Nielsen, K. K. Sand, J. D. Rodriguez-Blanco, N. Bovet, J. Generosi, K. N. Dalby and S. L. S. Stipp, *Cryst. Growth Des.*, 2016, **16**, 6199–6207.
78 D. Kralj, J. Kontrec, L. Brecevic, G. Falini and V. Nothig-Laslo, *Chem.–Eur. J.*, 2004, **10**, 1647–1656.
79 M. Suzuki, H. Nagasawa and T. Kogure, *Cryst. Growth Des.*, 2006, **6**, 2004–2006.
80 L. Addadi, S. Raz and S. Weiner, *Adv. Mater.*, 2003, **15**, 959–970.
81 Z. Liu and W. Meng, *J. CO2 Util.*, 2021, **44**, 101428.
82 D. Wang, C. Xiong, W. Li and J. Chang, *ACS Sustainable Chem. Eng.*, 2020, **8**, 14718–14731.
83 D. Aquilano, F. Otalora, L. Pastero and J. Manuel Garcia-Ruiz, *Prog. Cryst. Growth Charact.*, 2016, **62**, 227–251.

© 2022 The Author(s). Published by the Royal Society of Chemistry